Microdomain Ordering in Laterally Confined Block Copolymer Thin Films

August W. Bosse,[†] Carlos J. García-Cervera,[‡] and Glenn H. Fredrickson*[,§]

Department of Physics, University of California, Santa Barbara, California 93106, Polymers Division, National Institute of Standards and Technology, Gaithersburg, Maryland 20899, Department of Mathematics, University of California, Santa Barbara, California 93106, Department of Chemical Engineering, University of California, Santa Barbara, California 93106, Department of Materials, University of California, Santa Barbara, California 93106, and Materials Research Laboratory, University of California, Santa Barbara, California 93106

Received August 17, 2007; Revised Manuscript Received October 19, 2007

ABSTRACT: We examine the effects of small-scale, hexagonal, lateral confinement on microdomain ordering in diblock copolymer thin films using self-consistent field theory simulations. Specifically, we examine a hexagonal confinement well with side length L approximately equal to five cylindrical microdomain lattice spacings. The commensurability constraints of the small-scale, lateral confinement, coupled with surface-induced effects allow the confining well to have a significant effect on the perfection of microdomain order. We identify *commensurability windows* in L that depend on the segment−wall interaction and the "temperature" annealing rate (modeled as a Flory $\chi \sim 1/T$ annealing rate). The effect of added majority-block homopolymer is also explored.

1. Introduction

Block copolymer (BCP) thin films represent a promising tool for generating sub-optical lithographic patterns,[1−3] and as such, ordering of hexagonally packed microdomains in BCP thin films has received much attention in recent years.[4−8] In particular, there is considerable technological interest in using self-assembled BCP microdomain arrays in next-generation, sub-micrometer fabrication techniques.[9−11] A BCP thin film consisting of a large array of microphase-separated spheres or cylinders can be used to pattern a substrate yielding a large array of $\mathcal{O}$(10 nm) dots. Such dot arrays are potentially useful in next generation high-density magnetic media and semiconductor devices.[9] However, if such devices are to be realized, the dot arrays must exhibit high uniformity and order. This requirement translates into the need for large, quasi-2D arrays of uniform, well-ordered BCP microdomains.

Unfortunately, it is difficult to generate large, 2D arrays of uniform, well-ordered microdomains. While reasonably ordered micrometer-sized grains are often possible with exceptionally long thermal annealing times, recent work by Segalman et al. suggests that large 2D arrays of BCP microdomains exhibit equilibrium defect populations and defect-mediated melting transitions consistent with the Kosterlitz−Thouless−Halperin−Nelson−Young (KTHNY) theory of 2D melting.[4] Accordingly, defect formation in large 2D systems appears to be unavoidable.

There has also been substantial work on enhancing order in thin film block copolymer systems. Possible techniques for inducing order include applied external fields (e.g., electric, sheer, etc.) and lateral confinement, among others (for reviews of the various methods of enhancing order in BCP material, see refs 1−3). For example, Segalman et al. have examined the effects of a boundary on the ordering of hexagonally packed microdomains.[5,6] In short, they observed increased microdomain order inside of a region extending approximately 4.75 μm from the boundary [for the polystyrene-*b*-(2-vinylpyridine) system studied, with $N = 670$ and $f_{PVP} = 0.129$, this is approximately 160 microdomain lattice spacings]. In addition, Ross and co-workers have examined the effects of ordering and commensurability in small-scale confining channels and near confining corners.[3,12−14] These results suggest that template-directed assembly, and in particular lateral confinement represents a promising tool for controlling microdomain order in BCP systems.

In this paper, we present a computational study of small-scale, lateral confinement as a means of controlling microdomain order in thin film BCP systems. Motivated by recent work on hexagonally confined BCP thin films[15−18] and planned experiments involving small-scale confinement,[19] we focus on a hexagonally confined, cylinder-forming AB diblock copolymer thin film, both with and without added A homopolymer. The lateral size of the hexagonal confining well is selected such that nine cylinder rows fit across the hexagon (or, equivalently, five microdomains along an edge, giving a total of 61 enclosed microdomains). This size roughly corresponds to proposed experimental confinement sizes.[19] The size of the hexagonal confining well can be made to be commensurate with the hexagonal microdomain lattice formed by the bulk microphase-separated BCP. It is reasonable to suppose that the confinement will have a significant effect on ordering in the relatively small hexagonal array of microdomains.

The confined BCP system was simulated using a self-consistent field theory (SCFT) for polymer melts (for a more detailed account of SCFT, see ref 20) where the hexagonal confinement well was modeled as a fixed particle density (similar to the "masking" technique introduced by Matsen[21]). In our study, we varied the side length of the confining hexagon

* Corresponding author. E-mail: ghf@mrl.ucsb.edu.
[†] Department of Physics, University of California, Santa Barbara, and Polymers Division, National Institute of Standards and Technology.
[‡] Department of Mathematics, University of California, Santa Barbara.
[§] Departments of Chemical Engineering and Materials and Materials Research Laboratory, University of California, Santa Barbara.

10.1021/ma071866t CCC: $37.00
Published on Web 11/29/2007

and the sign of the segment−wall interaction to achieve either A- or B-block wetting.

We demonstrate that the side length has an appreciable effect on the ordering of the confined microdomains. Furthermore, we identify a "commensurability window" of side lengths such that a near-perfect, small-scale hexagonal array of microdomains is reproducibly obtained within the well. We examine the dependence of the window's width on the polymer−wall interaction, the temperature annealing rate (modeled via the Flory χ parameter), and the fraction of majority-block A homopolymer added to the copolymer. Finally, we explore the mechanisms by which the surfaces of the well induce order within the hexagonal domain.

Our presentation is outlined as follows. In section 2, we present the model and SCFT formalism for an AB + A + wall system. In section 3, we present our results and discussion. Specifically, in section 3.1, we examine the case of a quench to a fixed Flory χ parameter (analogous to a quench from infinite temperature to a temperature corresponding to χ). In section 3.2, we examine the effects of controlled temperature annealing (i.e., χ annealing) during the SCFT relaxation. In section 3.3, we examine and discuss the effects of a majority-block homopolymer additive. And finally, in section 4, we close with a short summary and concluding remarks.

2. Model and Methods

A blend of AB block copolymers, A homopolymers, and fixed wall "particles" is modeled using a standard Gaussian thread model with a Flory-type segment−segment and segment−wall interaction. The fixed wall field and segment−wall interaction are modeled using a method similar to that introduced by Matsen.[21] In section 2.1, we outline the AB + A + wall model, and in section 2.2, we outline our numerical methods.

2.1. Model and SCFT. We consider an incompressible melt of n_d monodisperse AB diblock copolymers, n_h monodisperse A homopolymers, and n_w wall "particles" in a volume V. The fraction of A-segments in the AB diblock is denoted f, the index of polymerization of the AB diblock is denoted $N_d = N$, and the index of polymerization of the A-homopolymer is denoted $N_h = \alpha N$, so that the parameter α is defined by the ratio $\alpha \equiv N_h/N$.

Each polymer is modeled as a continuous Gaussian chain characterized by space curves $\mathbf{r}_{di}(s)$ and $\mathbf{r}_{hj}(s)$, where $i = 1, 2, ..., n_d$ and $j = 1, 2, ..., n_h$ are polymer indices. For the AB diblock, the contour variable s runs from $s = 0$ at the beginning of the A-block end to $s = 1$ at the end of the B-block end, with $s = f$ corresponding to the end of the A block and the beginning of the B block. For the A homopolymer, s runs from $s = 0$ to $s = \alpha$. We assume the statistical segment lengths of the A and B segments are equal, $b_A = b_B = b$. Therefore, the unperturbed radius of gyration of the AB diblock is given by $R_{g0}^2 = b^2N/6$. The volume ν_0 occupied by A segments, B segments, and wall "particles" is given by $\nu_0 = 1/\rho_0$, where ρ_0 is the average total segment + wall density:

$$\rho_0 \equiv \frac{n_d N + n_h \alpha N + n_w}{V} \tag{1}$$

The AB + A + wall system is characterized by four microscopic densities. The microscopic diblock A-segment density is given by

$$\hat{\rho}_{Ad}(\mathbf{r}) = N \sum_{i=1}^{n_d} \int_0^f \mathrm{d}s\, \delta(\mathbf{r} - \mathbf{r}_{di}(s)) \tag{2}$$

the microscopic homopolymer A-segment density is given by

$$\hat{\rho}_{Ah}(\mathbf{r}) = N \sum_{j=1}^{n_h} \int_0^\alpha \mathrm{d}s\, \delta(\mathbf{r} - \mathbf{r}_{hj}(s)) \tag{3}$$

and the microscopic *total* A-segment density is defined by

$$\hat{\rho}_A(\mathbf{r}) = \hat{\rho}_{Ad}(\mathbf{r}) + \hat{\rho}_{Ah}(\mathbf{r}) \tag{4}$$

Likewise, the microscopic B-segment density is given by

$$\hat{\rho}_{Bd}(\mathbf{r}) = N \sum_{i=1}^{n_d} \int_f^1 \mathrm{d}s\, \delta(\mathbf{r} - \mathbf{r}_{di}(s)) \tag{5}$$

Finally, the microscopic wall "particle" density $\rho_w(\mathbf{r})$ is a predetermined, *fixed* function with $0 \le \rho_w(\mathbf{r}) \le \rho_0$, for all $\mathbf{r}$. We use this function to model a confinement well, and we often use the term *wall field* to refer to the microscopic wall "particle" density $\rho_w(\mathbf{r})$. Melt incompressibility requires that the microscopic densities locally sum up to the average total segment + wall density:

$$\hat{\rho}_A(\mathbf{r}) + \hat{\rho}_B(\mathbf{r}) + \rho_w(\mathbf{r}) = \rho_0 \tag{6}$$

Alternatively, we can express eq 6 as

$$\hat{\rho}_A(\mathbf{r}) + \hat{\rho}_B(\mathbf{r}) = \rho(\mathbf{r}) \tag{7}$$

where we have introduced the *fixed* total segment density

$$\rho(\mathbf{r}) = \rho_0 - \rho_w(\mathbf{r}) \tag{8}$$

In the canonical ensemble, the partition function of the AB + A + wall system is given by functional integrals over all configurations of all the polymer space curves:

$$Z = \int \prod_{i=1}^{n_d} \delta\mathbf{r}_{di} \prod_{j=1}^{n_h} \delta\mathbf{r}_{hj}\, \delta[\hat{\rho}_A + \hat{\rho}_B + \rho_w - \rho_0] \mathrm{e}^{-U_0 - U_I} \tag{9}$$

where

$$U_0 = \frac{1}{4R_{g0}^2} \sum_{i=1}^{n_d} \int_0^1 \mathrm{d}s \left|\frac{\mathrm{d}\mathbf{r}_{di}(s)}{\mathrm{d}s}\right|^2 + \frac{1}{4R_{g0}^2} \sum_{j=1}^{n_h} \int_0^\alpha \mathrm{d}s \left|\frac{\mathrm{d}\mathbf{r}_{hj}(s)}{\mathrm{d}s}\right|^2 \tag{10}$$

and

$$U_I = \frac{1}{\rho_0} \int_V \mathrm{d}\mathbf{r} [\chi \hat{\rho}_A(\mathbf{r}) \hat{\rho}_B(\mathbf{r}) - \chi_{wA} \rho_w(\mathbf{r}) \hat{\rho}_A(\mathbf{r}) - \chi_{wB} \rho_w(\mathbf{r}) \hat{\rho}_B(\mathbf{r})] \tag{11}$$

Here χ is the Flory parameter for A-segment−B-segment interactions, χ_{wA} is the Flory-like parameter for wall−A-segment interactions, and χ_{wB} is the Flory-like parameter for wall−B-segment interactions. In eq 9, $\delta[\hat{\rho}_A + \hat{\rho}_B + \rho_w - \rho_0]$ is a δ functional that enforces the incompressibility of the polymer melt at all points in the domain.

Note that

$$\chi_{wA} \hat{\rho}_A + \chi_{wB} \hat{\rho}_B = \chi_w \hat{\rho}_- + \frac{\chi_{wA}}{2} \hat{\rho}_+ + \frac{\chi_{wB}}{2} \hat{\rho}_+ \tag{12}$$

where

$$\chi_w \equiv \frac{\chi_{wA} - \chi_{wB}}{2} \tag{13}$$

$$\hat{\rho}_\pm = \hat{\rho}_A \pm \hat{\rho}_B \tag{14}$$

and we have dropped the explicit **r** dependence for clarity. Using eqs 12−14, and explicitly enforcing the incompressibility constraint, $\rho_+(\mathbf{r}) = \rho(\mathbf{r})$, gives

$$U_I = -\frac{\chi}{4\rho_0}\int_V d\mathbf{r}\left[\hat{\rho}_-(\mathbf{r}) + 2\frac{\chi_w}{\chi}\rho_w(\mathbf{r})\right]^2 \tag{15}$$

up to a constant shift in energy. We now write the interaction terms as follows (again, we elect to drop explicit **r** dependence),

$$e^{-U_I} = \exp\left[\frac{\chi}{4\rho_0}\int_V d\mathbf{r}\left(\hat{\rho}_- + 2\frac{\chi_w}{\chi}\rho_w\right)^2\right] = \int \delta_{w_-}\exp\left\{\int_V d\mathbf{r}\left[\left(\hat{\rho}_- + 2\frac{\chi_w}{\chi}\rho_w\right)w_- - \frac{\rho_0}{\chi}{w_-}^2\right]\right\} \tag{16}$$

We also represent the δ functional in eq 9 as a functional integral:

$$\delta[\hat{\rho}_+ - \rho] = \int \delta w_+ \exp[-i\int_V d\mathbf{r}\,(\hat{\rho}_+ - \rho)w_+] \tag{17}$$

After some manipulations, we arrive at the following expression for the partition function in terms of the conjugate potential fields $W_\pm = Nw_\pm$:

$$Z = \int \delta W_+ \delta W_- \, e^{-H[W_+, W_-]} \tag{18}$$

where

$$H[W_+, W_-] = C\int_V d\mathbf{x}\left[\frac{1}{\chi N}{W_-}^2(\mathbf{x}) - i\phi(\mathbf{x})W_+(\mathbf{x}) - 2\frac{\chi_w}{\chi}\phi_w(\mathbf{x})W_-(\mathbf{x})\right] - C(1-\varphi_h)\bar{\phi}V\log Q_d[W_A, W_B] - C\frac{\varphi_h\bar{\phi}V}{\alpha}\log Q_h[W_A] \tag{19}$$

Here $C \equiv \rho_0/N$, $\phi(\mathbf{x}) \equiv \rho(\mathbf{x})/\rho_0$, $\phi_w(\mathbf{x}) \equiv \rho_w(\mathbf{x})/\rho_0$, $W_A = iW_+ - W_-$, and $W_B = iW_+ + W_-$. Furthermore, *all* lengths have been scaled by the radius of gyration of the AB diblock copolymer where $\mathbf{x} = \mathbf{r}/R_{g0}$; for example, the system volume is expressed as a dimensionless variable, $V/{R_{g0}}^3 \rightarrow V$. The quantity $\bar{\phi} \equiv (1/V)\int_V d\mathbf{x}\,\phi(\mathbf{x}) = (n_dN + n_h\alpha N)/(n_dN + n_h\alpha N + n_w)$ represents the average *segment* volume fraction of the *entire* system (i.e., the volume fraction of the system that corresponds to polymer segments), and the quantity $\varphi_h = n_h\alpha N/(n_dN + n_h\alpha N)$ represents the fraction of segments that belong to A homopolymers.

The single-chain partition functions $Q_d[W_A, W_B]$ and $Q_h[W_A]$ can be expressed in terms of the "forward propagators" $q_d(\mathbf{x}, s; [W_A, W_B])$ and $q_h(\mathbf{x}, s; [W_A, W_B])$ as follows:

$$Q_d[W_A, W_B] = \frac{1}{V}\int d\mathbf{x}\, q_d(\mathbf{x}, 1; [W_A, W_B]) \tag{20}$$

and

$$Q_h[W_A, W_B] = \frac{1}{V}\int d\mathbf{x}\, q_h(\mathbf{x}, \alpha; [W_A, W_B]) \tag{21}$$

where $q_d(\mathbf{x}, s; [W_A, W_B])$ satisfies

$$\frac{\partial}{\partial s}q_d(\mathbf{x}, s; [W_A, W_B]) = \nabla^2 q_d(\mathbf{x}, s; [W_A, W_B]) - \psi_d(\mathbf{x}, s)q_d(\mathbf{x}, s; [W_A, W_B]) \tag{22}$$

subject to the initial condition $q_d(x, 0; [W_A, W_B]) = 1$ with

$$\psi_d(\mathbf{x}, s) = \begin{cases} W_A(\mathbf{x}), & 0 < s < f \\ W_B(\mathbf{x}), & f < s < 1 \end{cases} \tag{23}$$

and $q_h(\mathbf{x}, s; [W_A, W_B])$ satisfies

$$\frac{\partial}{\partial s}q_h(\mathbf{x}, s; [W_A, W_B]) = \nabla^2 q_h(\mathbf{x}, s; [W_A, W_B]) - W_A(\mathbf{x})q_h(\mathbf{x}, s; [W_A, W_B]) \tag{24}$$

subject to the initial condition $q_h(\mathbf{x}, 0; [W_A, W_B]) = 1$. The average microscopic volume fractions ϕ_{Ad}, ϕ_{Ah}, and ϕ_B can be expressed as integrals over the propagators:

$$\phi_{Ad}(\mathbf{x}; [W_A, W_B]) = \frac{(1-\varphi_h)\bar{\phi}}{Q_d}\times \int_0^f ds\, q_d(\mathbf{x}, s; [W_A, W_B])q_d^\dagger(\mathbf{x}, 1-s; [W_A, W_B]) \tag{25}$$

$$\phi_{Ah}(\mathbf{x}; [W_A, W_B]) = \frac{\varphi_h\bar{\phi}}{\alpha Q_h}\int_0^\alpha ds\times q_h(\mathbf{x}, s; [W_A, W_B])q_h(\mathbf{x}, \alpha - s; [W_A, W_B]) \tag{26}$$

and

$$\phi_B(\mathbf{x}; [W_A, W_B]) = \frac{(1-\varphi_h)\bar{\phi}}{Q_d}\times \int_f^1 ds\, q_d(\mathbf{x}, s; [W_A, W_B])q_d^\dagger(\mathbf{x}, 1-s; [W_A, W_B]) \tag{27}$$

where the "backward propagator" $q_d^\dagger(\mathbf{x}, s; [W_A, W_B])$ satisfies the following differential equation

$$\frac{\partial}{\partial s}q_d^\dagger(\mathbf{x}, s; [W_A, W_B]) = \nabla^2 q_d^\dagger(\mathbf{x}, s; [W_A, W_B]) - \psi_d^\dagger(\mathbf{x}, s)q_d^\dagger(\mathbf{x}, s; [W_A, W_B]) \tag{28}$$

subject to the initial condition $q_d^\dagger(\mathbf{x}, 0; [W_\pm]) = 1$ with

$$\psi_d^\dagger(\mathbf{x}, s) = \begin{cases} W_B(\mathbf{x}), & 0 < s < 1-f \\ W_A(\mathbf{x}), & 1-f < s < 1 \end{cases} \tag{29}$$

In the formal $C \rightarrow \infty$ limit, we use the saddle-point approximation to find mean-field configurations of the conjugate fields $W_\pm$. The saddle point equations are given by the standard expressions:

$$\left.\frac{\delta H[W_+, W_-]}{\delta W_+(\mathbf{x})}\right|_{\tilde{W}_\pm} = iC[\phi_{Ad}(\mathbf{x}; [\tilde{W}_\pm]) + \phi_{Ah}(\mathbf{x}; [\tilde{W}_\pm]) + \phi_B(\mathbf{x}; [\tilde{W}_\pm]) - \phi(\mathbf{x})] = 0 \tag{30}$$

and

$$\left.\frac{\delta H[W_+, W_-]}{\delta W_-(\mathbf{x})}\right|_{\tilde{W}_\pm} = C[(2/\chi N)\tilde{W}_-(\mathbf{x}) - 2(\chi_w/\chi)\phi_w(\mathbf{x}) - \phi_{Ad}(\mathbf{x}; [\tilde{W}_\pm]) - \phi_{Ah}(\mathbf{x}; [\tilde{W}_\pm]) + \phi_B(\mathbf{x}; [\tilde{W}_\pm])] = 0 \tag{31}$$

where $\tilde{W}_\pm$ are the saddle point values of $W_\pm$. The saddle point

value of W_+ is strictly imaginary, and the saddle point value of W_- is strictly real.[22,20] Accordingly, we define a real valued *pressure* field $\Xi = i\tilde{W}_+ = -\mathrm{Im}[\tilde{W}_+]$ and a real valued *composition* field $W = \tilde{W}_- = \mathrm{Re}[\tilde{W}_-]$. This gives the following saddle point equations:

$$\phi_{\mathrm{Ad}}(\mathbf{x}) + \phi_{\mathrm{Ah}}(\mathbf{x}) + \phi_{\mathrm{B}}(\mathbf{x}) - \phi(\mathbf{x}) = 0 \tag{32}$$

and

$$(2/\chi N)W(\mathbf{x}) - 2(\chi_{\mathrm{w}}/\chi)\phi_{\mathrm{w}}(\mathbf{x}) - \phi_{\mathrm{Ad}}(\mathbf{x}) - \phi_{\mathrm{Ah}}(\mathbf{x}) + \phi_{\mathrm{B}}(\mathbf{x}) = 0 \tag{33}$$

We solve these equations by introducing a fictitious "time" variable t and relaxing the fields forward in time in the direction of the thermodynamic forces. This "steepest descent" saddle point search is formally given by

$$\frac{\partial}{\partial t}\Xi(\mathbf{x}, t) = \frac{\delta H[\Xi, W]}{\delta \Xi(\mathbf{x}, t)} \tag{34}$$

$$\frac{\partial}{\partial t}W(\mathbf{x}, t) = -\frac{\delta H[\Xi, W]}{\delta W(\mathbf{x}, t)} \tag{35}$$

Clearly, eqs 32 and 33 are satisfied when eqs 34 and 35 are stationary.

The fictitious time, continuous steepest descent search given by eqs 34 and 35 is not the only possible SCFT update capable of yielding saddle point solutions. For example, quasi-dynamic[23,24] variants of the steepest descent search exist that can provide qualitative and in some cases quantitative information about the kinetic pathway to equilibrium, albeit at the expensive of significantly increased computational cost. A discussion of such "dynamic SCFT" methods is beyond the scope of this paper; specifically, here we are interested in equilibrium and metastable saddle point configurations of the BCP melt. The steepest descent search summarized by eqs 34 and 35 has been demonstrated to be an effective means of identifying physically relevant saddle point solutions[20] and will thus be adopted for this study.

This completes the standard framework for the SCFT of an AB + A + wall system. The mean-field configurations Ξ and W are found by iterating the following scheme:

1. Initialize the pressure and composition fields, $\Xi(\mathbf{x}, 0)$ and $W(\mathbf{x}, 0)$.
2. Solve the modified diffusion equations for $q_{\mathrm{d}}(\mathbf{x}, s)$, $q_{\mathrm{d}}^{\dagger}(\mathbf{x},s)$, and $q_{\mathrm{h}}(\mathbf{x},s)$.
3. Calculate Q_{d}, Q_{h}, ϕ_{Ad}, ϕ_{Ah}, and ϕ_{B}.
4. Update $\Xi(\mathbf{x}, t)$ and $W(\mathbf{x}, t)$ by integrating eqs 34 and 35 forward over a time interval Δt.
5. Repeat steps 2−5 until a convergence criterion has been met.

More complete details of the Gaussian thread model and polymer SCFT can be found in ref 20.

The wall field $\phi_{\mathrm{w}}(\mathbf{x}) = \rho_{\mathrm{w}}(\mathbf{x})/\rho_0$ is a fixed function of $\mathbf{x}$ that is specified before starting the SCFT simulations. We select $\phi_{\mathrm{w}}(\mathbf{x})$ to be a regular hexagonal pattern centered about the midpoint of the simulation space. The interior of the hexagon is set to $\phi_{\mathrm{w}}(\mathbf{x}) = 0$, and the exterior of the hexagon is set to $\phi_{\mathrm{w}}(\mathbf{x}) = 1$, with a narrow, smooth transition region connecting the interior and exterior. The incompressibility constraint eq 6 restricts polymer segments to the interior of the hexagon. In other words, the fixed wall field $\phi_{\mathrm{w}}(\mathbf{x})$ acts as a confinement well for the segments of the fluid.

In order to minimize the number of required Fourier modes needed to resolve the $\phi_{\mathrm{w}}(\mathbf{x}) = 0$ to $\phi_{\mathrm{w}}(\mathbf{x}) = 1$ transition region, and in order to retain the stability characteristics of standard saddle point search methods (to be discussed below), the transition is selected to be a hyperbolic tangent form:

$$\phi_{\mathrm{w}}(\mathbf{x}) = \frac{1}{2}\left[1 + \tanh\left(z\frac{d_{\perp}(\mathbf{x})}{\delta}\right)\right] \tag{36}$$

Here z and δ are factors used to define the transition region and set the width of the transition region, respectively, and $d_{\perp}(\mathbf{x})$ is defined as the distance from the point $\mathbf{x}$ to the nearest edge of the boundary of the hexagonal well. The boundary of the hexagonal well is defined to be at the midpoint of the smooth transition region (i.e., where $\phi_{\mathrm{w}}(\mathbf{x}) = 1/2$). We select z such that the wall transition region is defined to begin at $\phi_{\mathrm{w}}(\mathbf{x}) = 0.01$ and end at $\phi_{\mathrm{w}}(\mathbf{x}) = 0.99$ with a width of δ. This gives $z = \log(99) \approx 4.5951$. We do not expect the specific value of δ selected to affect the results, provided that δ is approximately equal to the AB interface width (i.e., a fraction of $1R_{g0}$).

2.2. Numerical Methods. In order to examine the effects of *lateral* confinement on the BCP melt, we simulate the AB + A + wall system in 2D. We sample all relevant fields on a square, periodic lattice in x and y:

$$\begin{aligned} x_i &= i\Delta x \quad i = 0, ..., n_x - 1 \\ y_j &= j\Delta y \quad j = 0, ..., n_y - 1 \end{aligned} \tag{37}$$

where n_x and n_y are the number of lattice points in the x and y directions, respectively, $\Delta x = L_x/n_x$ and $\Delta y = L_y/n_y$ are the grid spacings, L_x is the length of the system in the x direction, and L_y is the length of the system in the y direction. We will subsequently use a single, bold-face index $\mathbf{i}$ to represent the ordered pair (i, j). It is important to note that the above-defined discretization represents a uniform collocation grid allowing for the use of fast Fourier transforms (FFTs).

The system is assumed to be uniform but finite in the z direction, and the film thickness is denoted L_z. Under this assumption, the film thickness always appears as a constant factor in combination with C. In SCFT, the factor of C, and thus L_z, is absorbed into the relaxation time step Δt, discussed below. With the above-defined simulation space, the volume of the system is denoted $V = L_xL_yL_z$ and the total number of lattice points is given by $M = n_xn_y$.

Provided that the top and bottom surfaces do not have a selective interaction with the BCP melt, our simulation methodology should provide useful insight into the effects of small-scale, *lateral* confinement on BCP microdomain ordering. In order to simulate more complicated situations where the top and bottom surfaces of a BCP film have a selective interaction with the two blocks, a full 3D simulation framework would be required.

We also discretize the chain contour variable s:

$$s_m = m\Delta s,\ m = 0, ..., n_s \tag{38}$$

where n_s is the number of steps along the polymer backbone, and $\Delta s = 1/n_s$ is the contour step size. The fictitious time variable t is also discretized:

$$t_n = n\Delta t, \quad n = 0, ..., n_{\mathrm{t}} \tag{39}$$

The value of Δt selected depends on the method used to solve the relaxation equations (discussed below), and n_{t} defines the total number of SCFT iterations used to relax the saddle point equations.

In step 2 of the SCFT algorithm, outlined in section 2.1, we solve the modified diffusion equations using the pseudo-spectral

operator splitting method developed by Rasmussen and coworkers.[25,26] That is, motivated by both the formal solution

$$q(\mathbf{x}, s + \Delta s) = e^{\Delta s \mathscr{L}} q(\mathbf{x}, s) \tag{40}$$

with the initial condition $q(\mathbf{x}, 0) = 1$, and the Baker−Campbell−Hausdorff identity,[27] we perform an $\mathcal{O}(\Delta s^2)$ splitting of $e^{\Delta s \mathscr{L}}$:

$$e^{\Delta s \mathscr{L}} = e^{-\Delta s \psi(\mathbf{x},s)/2} e^{\Delta s \nabla^2} e^{-\Delta s \psi(\mathbf{x},s)/2} + \mathcal{O}(\Delta s^3) \tag{41}$$

where $\mathscr{L} \equiv \nabla^2 - \psi(\mathbf{x}, s)$. The function $\psi(\mathbf{x}, s)$ is diagonal in real space, and the Laplacian operator is diagonal in Fourier space; thus, $e^{-\Delta s \psi(\mathbf{x},s)/2}$ is evaluated in real space and $e^{\Delta s \nabla^2}$ in Fourier space. As mentioned above, the collocation grid allows us to move between real and Fourier space using FFTs.

The time integration of eqs 34 and 35 is performed using an explicit, forward-Euler algorithm:

$$\Xi_{\mathbf{i}}^{n+1} = \Xi_{\mathbf{i}}^{n} + \Delta t \frac{\partial H[\Xi^n, W^n]}{\partial \Xi_{\mathbf{i}}^{n}} \tag{42}$$

$$W_{\mathbf{i}}^{n+1} = W_{\mathbf{i}}^{n} - \Delta t \frac{\partial H[\Xi^n, W^n]}{\partial W_{\mathbf{i}}^{n}} \tag{43}$$

where superscripts n represent discrete steps in the time variable t. As indicated above, C and L_z are constant factors in the Hamiltonian $H[\Xi^n, W^n]$; therefore, they represent a modification to the Euler time step Δt. Henceforth, we use the symbol Δt to represent the total time step $\Delta t C L_z$.

We use as a convergence criterion the L_1 norm of the sum of the thermodynamic forces at SCFT iteration n:[28]

$$\left| \frac{\delta H[\Xi^n, W^n]}{\delta \Xi^n} + \frac{\delta H[\Xi^n, W^n]}{\delta W^n} \right|_1 = \frac{1}{M} \sum_{\mathbf{i}}^{M} \left| \frac{\partial H[\Xi^n, W^n]}{\partial \Xi_{\mathbf{i}}^{n}} + \frac{\partial H[\Xi^n, W^n]}{\partial W_{\mathbf{i}}^{n}} \right| \tag{44}$$

Clearly, a completely relaxed saddle point solution gives $|\delta H/\delta \Xi + \delta H/\delta W|_1 = 0$.

3. Results and Discussion

In order to examine how hexagonal, lateral confinement affects ordering in block copolymer thin films, we simulated AB + A + wall systems in 2D using SCFT, as discussed above. The results of these simulations are presented below.

For all simulations we set $f = 0.7$—*with this choice we identify the A block as the majority block.*[39] For the quenched simulations presented in section 3.1, χN was held fixed at $\chi N = 17$. This value of f and χN yields saddle point solutions corresponding to a hexagonally ordered cylindrical microphase. For the χN annealing simulations presented in section 3.2, χN was ramped from $\chi N = 12$ to the final value of $\chi N = 17$. The value of $\chi_w N$ was selected to be $\chi_w N = 17$, $\chi_w N = 0$, or $\chi_w N = -17$ for A-attractive, neutral, or B-attractive walls, respectively. For the AB diblock simulations (sections 3.1 and 3.2), the A homopolymer fraction was set to $\varphi_h = 0$, and for the AB + A blend simulations (section 3.3), the A homopolymer fraction was set to $\varphi_h = 0.20$, indicating that the blend is 20% A homopolymer. The A homopolymer length was selected to be 35% percent of the copolymer length, $\alpha = 0.35$.

The system size was chosen as $L_x = L_y = 48$; this system size allowed us to explore a wide range of possible hexagon sizes, up to a maximum hexagon side length of approximately $L = 24$. The wall transition region width was selected to be $\delta = 1$. We were interested in hexagon side lengths that yielded nine rows of microdomains across the hexagon, or equivalently five microdomains along an edge. There are exactly 61 microdomains contained in such a confining hexagon. With this in mind we focused on a range of hexagon side lengths between $L = 14.00$ and $L = 23.00$.

The spatial resolution was selected in order to resolve both the A−B interfaces and the wall transition region. We found that $\Delta x = \Delta y = 0.25$ was a sufficient resolution for our purposes; therefore, we set $n_x = n_y = 192$. The number of polymer contour steps was selected to be $n_s = 50$. These parameters allowed for sufficiently accurate evaluation of the energy functional (Hamiltonian) $H[\Xi, W]$ in order to differentiate between the various systems of interest (specifically, the various values of hexagon side length L).

For all simulations presented here, the Euler SCFT time step was selected to be $\Delta t = 2$. Larger time steps resulted in stability problems. The total number of SCFT iterations was set to $n_t = 20\,000$, unless otherwise indicated. For the Euler update discussed above, with $\Delta t = 2$ and $n_t = 20\,000$, we were able to determine the saddle point solutions Ξ and W with $|\delta H/\delta \Xi + \delta H/\delta W|_1 = \mathcal{O}(10^{-5})$. Using the above simulation parameters ($n_x = n_y = 192$, $n_s = 50$, and $n_t = 20\,000$), the average single simulation run time was approximately 7 h on a dedicated compute node. A total of 935 full production runs were carried out giving a total of approximately 6545 compute-hours.[40]

In order to identify the window in L that yielded a well-ordered array of microdomains (henceforth called the *commensurability window*), we measured the average standard deviation (SD) of nearest neighbor (NN) microdomain separations inside the confining hexagon $\langle\sigma\rangle$. This average was calculated from five or ten independent simulations, started from five or ten distinct random initial conditions (we used ten independent initial conditions for our quenched simulations and five independent initial conditions for our annealed simulations). When defects form, the nearest neighbor separation between microdomains will change locally (near the defects). Therefore, we expect to see a defect-induced jump in the standard deviation of nearest neighbor microdomain separations. We use the notation $\Lambda_{\mathcal{N}}(\chi_w N)$ to represent the commensurability window with exactly $\mathcal{N}$ enclosed microdomains for a specific value of $\chi_w N$.

For side lengths L outside of the commensurability window, we observed microdomain defect formation as a result of deviations from *exactly* $\mathcal{N} = 61$ enclosed microdomains discussed above. Accordingly, a deviation from 61 enclosed microdomains indicates a defective array. However, the jump in $\langle\sigma\rangle$ is much more abrupt (nearly an order of magnitude in $\langle\sigma\rangle$ over a change in hexagon side length of $\Delta L \approx 0.50$), and thus we use $\langle\sigma\rangle$ as our primary metric for identifying commensurability windows.

3.1. AB Quenched Simulations. Here we present results for a quench to $\chi N = 17$ (modeled as a SCFT relaxation from random initial conditions at a fixed $\chi N = 17$) for the AB + wall system presented above. There is no A homopolymer present in this system, so we set $\varphi_h = 0$.

In Figure 1, we present graphs of $\langle\sigma\rangle$ vs L for the AB diblock system with an A-attractive wall ($\chi_w N = 17$), neutral wall ($\chi_w N = 0$), and B-attractive wall ($\chi_w N = -17$). Recall, for $f = 0.7$, *the A block is the majority block.* From Figure 1a we see that the commensurability window for the A-attractive wall is given by $\Lambda_{61}(17) = [15.75, 17.00]$. This window defines the region

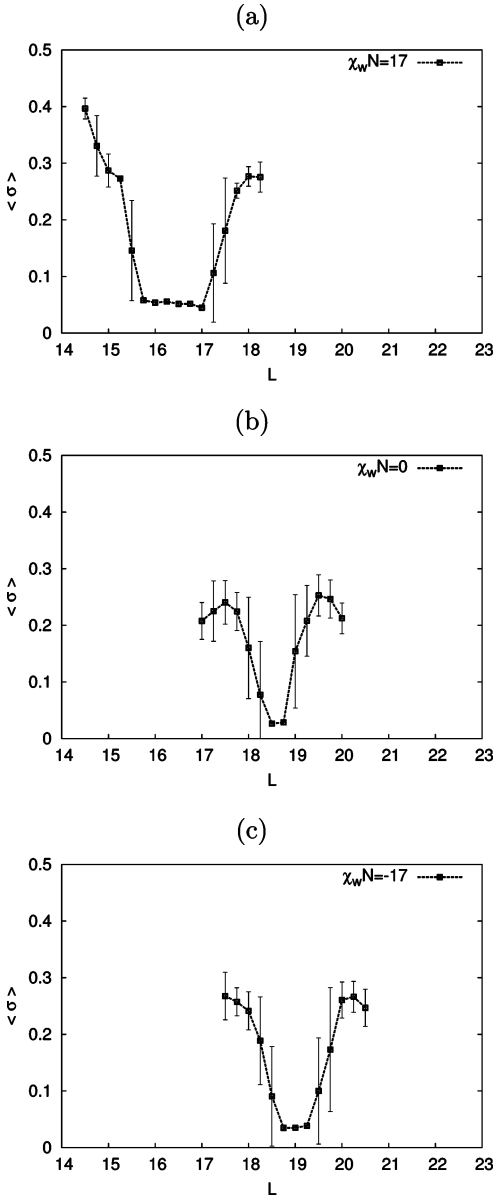

Figure 1. Graphs of $\langle\sigma\rangle$ vs L for an AB melt after a quench from random initial conditions to $\chi N = 17$ for (a) an A-attractive wall ($\chi_w N = 17$), (b) a neutral wall ($\chi_w N = 0$), and (c) an B-attractive wall ($\chi_w N = -17$). For each case, there is a region in L (the commensurability window) inside which there is a perfect array of 61 hexagonally ordered microdomains.

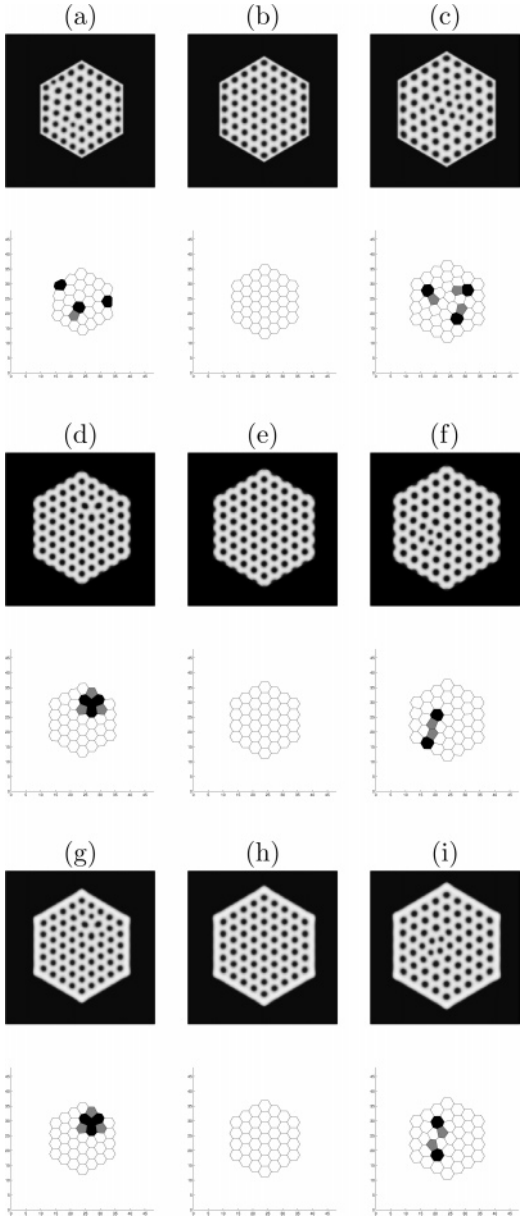

Figure 2. Representative composition profiles (lighter shades correspond to larger values of ϕ_A) and their corresponding Voronoi diagrams (hexagon in white, pentagon in gray, and heptagon in black) for (a−c) an A-attractive wall, (d−f) a neutral wall, and (g−i) a B-attractive wall. For the A-attractive wall, we plot composition profiles and their corresponding Voronoi diagrams for (a) $L = 15.00$, (b) $L = 16.25$, and (c) $L = 17.75$. For the neutral wall, we plot composition profiles and their corresponding Voronoi diagram for (d) $L = 17.75$, (e) $L = 18.50$, and (f) $L = 19.50$. Finally, for the B-attractive wall, we plot composition profiles and their corresponding Voronoi diagram for (g) $L = 18.00$, (h) $L = 19.00$, and (i) $L = 20.00$.

in L inside which we observed a well-ordered, hexagonal array of 61 microdomains for *all* 10 sampled random initial conditions and high uniformity in microdomain size and shape. For L inside of the commensurability window $\langle\sigma\rangle \approx 0.05$, and outside the window $\langle\sigma\rangle$ is larger by approximately 1 order of magnitude. From Figure 1b we see that the commensurability window for the neutral wall is given by $\Lambda_{61}(0) = [18.50, 18.75]$. Finally, from Figure 1c, we see that the commensurability window for the B-attractive wall is given by $\Lambda_{61}(-17) = [18.75, 19.25]$.

In Figure 2, we present representative compositions profiles and their corresponding Voronoi diagrams for A-attractive, neutral, and B-attractive walls. The composition profiles and Voronoi diagrams indicate the presence of defects for values of L outide of $\Lambda_{61}(\chi_w N)$ and the presence of a well-ordered array for values of L inside of $\Lambda_{61}(\chi_w N)$.

It is important to note that the commensurability windows identified for the neutral and B-attractive walls are considerably smaller than the commensurability window identified for the A-attractive wall. In fact, the commensurability window for the A-attractive wall is 2.5 times larger than the window for the B-attractive wall and five times larger than the window for the neutral wall. Furthermore, there appears to be a tendency for the defects to form along the confining wall for $L < \min[\Lambda_{61}(\chi_w N)]$ and in the center of the hexagon for $L > \max[\Lambda_{61}(\chi_w N)]$. The above identification of commensurability windows may have important technological applications. The simulation results suggest that if one can engineer a confining wall that attracts the majority block, then one may be able to exploit wider tolerances in L when constructing a confining hexagon.

It is not immediately obvious why the commensurability window for a majority-block-attractive wall should be wider than the window for neutral or minority-block-attractive walls. We can gain some insight into this observation by examining microphase development near the wall.

The above simulations essentially model a quench to a temperature corresponding to $\chi N = 17$.[29] In the bulk (i.e., far away from a wall), there are two particularly important values of χN for an asymmetric diblock (i.e., $f \neq 0.5$). First, there is the microphase separation transition (MST) value,[30] denoted $(\chi N)_{MST}$. Second, there is the spinodal value, denoted $(\chi N)_S$.[30] For the diblock system of interest in this paper, with $f = 0.7$, $(\chi N)_S \approx 15$ and $(\chi N)_{MST} \approx 14.75$.[30] If χN is selected to be below the MST value $\chi N < (\chi N)_{MST}$ then the composition profiles in a bulk simulation will rapidly relax to a homogeneous (also called disordered) state with $\phi_A(\mathbf{x}) = f$ and $\phi_B(\mathbf{x}) = 1 - f$. For a bulk simulation with $(\chi N)_{MST} < \chi N < (\chi N)_S$, the homogeneous (disordered) phase is metastable, and microphase separation can proceed via nucleating of the ordered phase (for a discussion of nucleation of the lamellar microphase in BCP systems, see refs 31 and 32). In this metastable region, the disordered phase BCP scattering function $S(k)$ is strongly peaked around $k = k_0$, corresponding to the periodicity of the microphase.[30] Finally, as χN approaches $(\chi N)_S$, the disordered phase scattering function diverges at k_0, the homogeneous phase becomes unstable (i.e., nucleation barriers vanish), and the system rapidly microphase separates.[30] In other words, for $\chi N > (\chi N)_S$, we expect rapid, global microphase separation on a length scale corresponding to $2\pi/k_0$. For symmetric diblock copolymers ($f = 0.5$) in the mean-field limit ($C \rightarrow \infty$), the values of $(\chi N)_{MST}$ and $(\chi N)_S$ coincide, and for weakly asymmetric diblocks, the values are nearly co-incident.

Microphase development of asymmetric BCPs near a boundary is complicated and rather subtle.[33−38] Accordingly, when necessary we draw comparisons from work on symmetric and weakly asymmetric BCPs. For example, Fredrickson showed that if a boundary has a preferential attraction to one component of a symmetric or weakly asymmetric diblock copolymer, one observes low-amplitude composition oscillations that extend into the bulk, with a magnitude that dies off exponentially.[33] These composition oscillations are observed in the disordered (homogeneous) phase, for temperatures well above the spinodal temperature [or equivalently, $\chi N < (\chi N)_S$]. As the system is cooled toward the spinodal temperature, the composition oscillations increase in magnitude and penetration depth, extending increasingly far into the bulk.[33] As $\epsilon = |\chi N - (\chi N)_S|/(\chi N)_S \rightarrow 0$, the magnitude of the composition oscillations approach the bulk microphase separation values, yielding a "wetting layer" with thickness $w \propto \log \epsilon$ that diverges logarithmically as $\epsilon \rightarrow 0$ (e.g., see ref 37).

For quenches into the ordered phase [i.e., $\chi N > (\chi N)_S$], Brown and Chakrabarti demonstrated that composition oscillations form near the boundary and propagate into the bulk.[36] Furthermore, they showed that the long-time form of the quenched $\chi N > (\chi N)_S$ composition profiles are well fit by the functional form identified by Fredrickson in ref 31 for $\chi N < (\chi N)_S$ composition oscillations.[36]

For the block copolymer system of interest here, the B segments microphase-separate to form a microdomain lattice. Therefore, it is useful to examine the order parameter

$$\psi(\mathbf{x}, t) = \phi_B(\mathbf{x}, t) - (1 - f)\phi(\mathbf{x}) \tag{45}$$

where as discussed above, $\phi(\mathbf{x}) = 1 - \phi_w(\mathbf{x})$ is the fixed total segment fraction function. In Figure 3, we plot $\psi(x, y, t)$ vs x at $y = 24$ [i.e., $\psi(x, 24, t)$ vs x], averaged over ten independent random initial conditions, for a AB diblock quenched to $\chi N = 17$, and confined by a $L = 17.75$ hexagonal wall. The line $y = 24$ is a perpendicular bisector of two opposite edges of the confining hexagon. The order parameter $\psi(x, 24, t)$ is plotted at iteration times $t = 20\Delta t$, $40\Delta t$, and $80\Delta t$ during the saddle point search. Here we only plot the A-attractive and B-attractive wall interactions. We can clearly see composition oscillations near the boundary at $x \approx 8.6$. These oscillations extend into the center of the hexagon and appear to rapidly decay. The shape and time dependence of the composition oscillations appears to be consistent with the surface-induced microphase separation phenomena referenced above.[36]

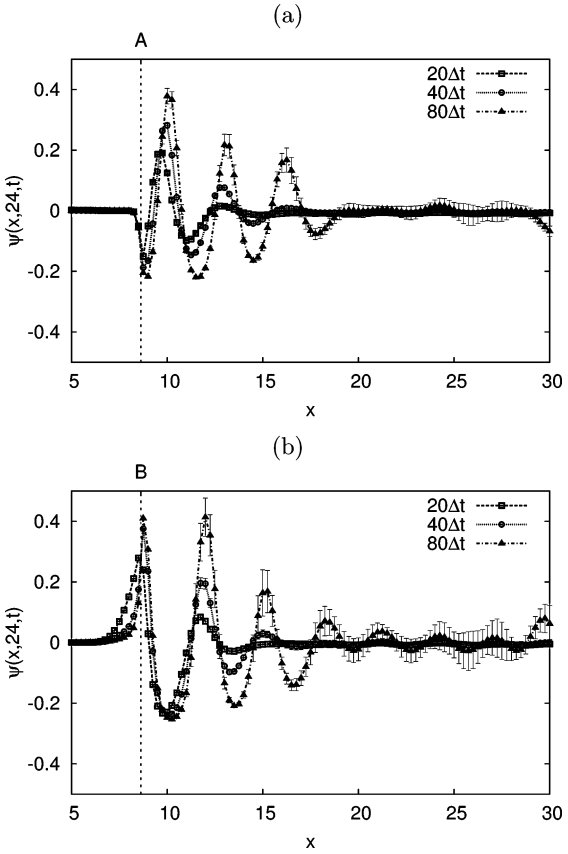

Figure 3. Graphs of $\psi(x, 24, t)$ vs x, averaged over ten independent random initial conditions, for (a) A-attractive wall (at point "A") and (b) B-attractive wall (at point "B"). In both figures, we plot $\psi(x, 24, t)$ at $t = 20\Delta t$ (square + dashed), $40\Delta t$ (circle + dotted), and $80\Delta t$ (triangle + dashed-dotted).

Of primarily importance in Figure 3 is the observation that, *when ignoring the surface enrichment layer*, the first peak in ψ *inside* of the boundary is *larger* for the A-attractive wall than for the B-attractive wall. The first peak in ψ *inside* of the boundary corresponds to the first interior cylinder-like B microdomain. The additional peaks in ψ that are even further inside the well are also larger for the A-attractive wall. Furthermore, we can see that all of the interior composition peaks remain larger for the A-attractive wall over all times reported in Figure 3. In Figure 4, we superimpose plots of $\psi(x, 24, t)$ vs x for A-attractive and B-attractive walls, averaged over 10 independent random initial conditions. We also shift the order parameter curves in Figure 4 so that the first interior composition peaks (not the surface enrichment layer) are aligned. With the order parameter curves superimposed and aligned, the larger peaks in ψ for the A-attractive wall are more easily identified. The difference in peak size is due to the rapid decay envelope.[33,36] For the case where A-segment is attracted to the wall,

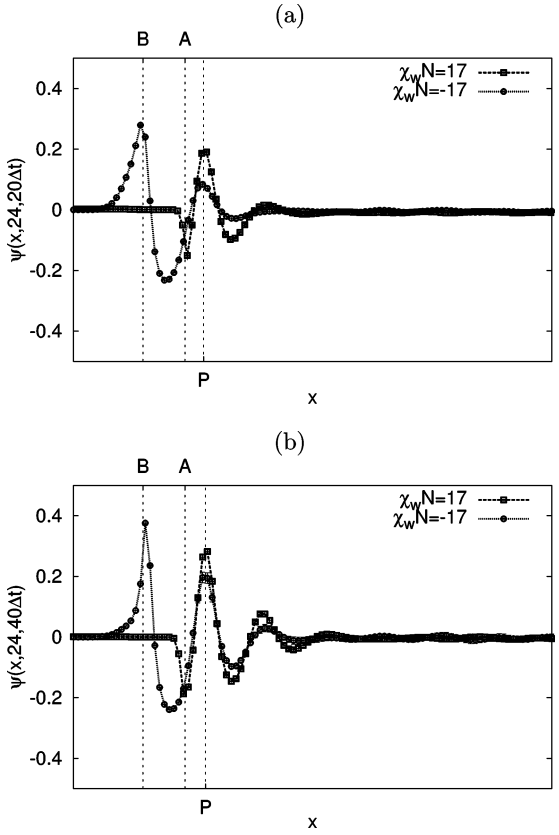

Figure 4. Shifted graphs of $\psi(x, 24, t)$ vs x, averaged over ten independent random initial conditions, at (a) $t = 20\Delta t$ and (b) $40\Delta t$. In both figures, we plot $\psi(x, 24, t)$ for an A-attractive wall (square + dashed) and a B-attractive wall (circle + dotted). The A- and B-attractive wall positions are marked as "A" and "B," respectively. The $\psi(x, 24, t)$ curves have been shifted in x so that the first interior order parameter peaks (at point "P") are aligned. This allows for an easy visual comparison of the peak heights.

the *polymer architecture* dictates that the first B microdomain forms much closer to the wall than for the B-attractive wall; accordingly, during the early stages of microphase separation near the surface, the amplitude for the positive peaks in ψ will be larger for the A-attractive wall.

The positive peaks in ψ correspond to points of increased B-segment fraction. The microphase-separated B microdomains form at or around these locations. Since the peaks in ψ are larger in amplitude for the A-attractive walls, we expect the A-attractive wall to have more influence over the enclosed B microdomains than the B-attractive wall. This is precisely what is illustrated in Figure 1.

Even though the resulting microphases have similar lattice constants (i.e., nearest neighbor separations), as can be appreciated in Figure 2, the polymer architecture also dictates that the confinement scale for the A-attractive wall is smaller than for the neutral or B-attractive wall (see Figure 2). This smaller-scale confinement, coupled with the architectural dependencies of surface-induced phase separation, suggests that the A-attractive wall will have more influence over the B microdomain formation (and thus ordering), when compared to neutral or B-attractive walls.

We have largely ignored the neutral wall up until this point. This is because the neutral wall appears to both quantitatively (Figure 1) and qualitatively (Figure 2) resemble the B-attractive wall. That is, the B segments are attracted to the neutral wall much like the B-attractive wall, and the size and width of the commensurability windows are similar for the neutral and B-attractive walls.

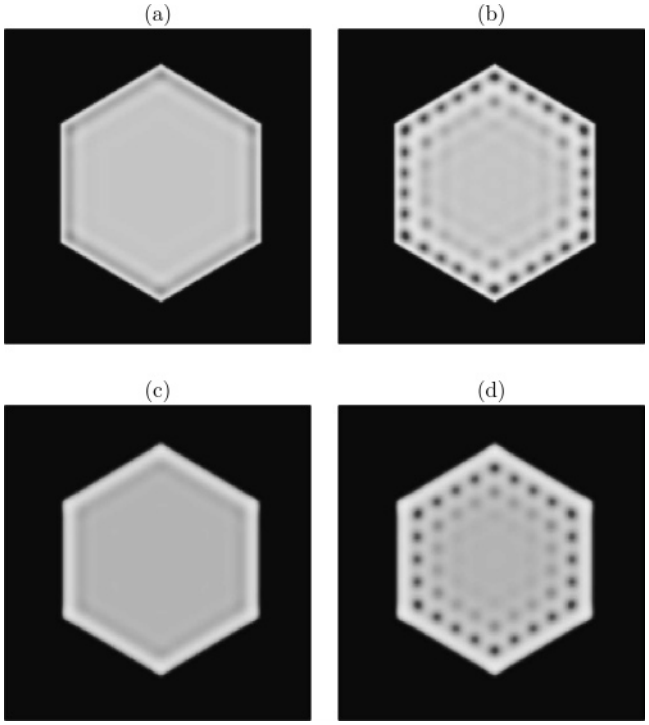

Figure 5. Representative *equilibrium* density composition profiles (lighter shades correspond to larger values of ϕ_A) for (a) A-attractive wall at $\chi N = 12$, (b) A-attractive wall at $\chi N = 14$, (c) B-attractive wall at $\chi N = 12$, and (d) B-attractive wall at $\chi N = 14$.

In addition to the wall's role in surface-induced microphase separation phenomena, the shape of the well helps orient the microdomains in a way that is commensurate with a hexagonal lattice. Provided the hexagon side length is carefully selected [i.e., $L \in \Lambda_1(\chi_w N)$], the hexagonal shape of the boundary will work to encourage the surface-induced composition waves to form a well-ordered hexagonal microphase array.

We noted above that for L below the observed commensurability windows, defects tend to form along the wall. This is most likely due to direct incommensurability effects. That is, the side length is not commensurate with the natural microdomain cylinder spacing. In contrast, for L above the ordered window, defects primarily form inside the confining hexagon. This kind of defect formation likely involves incommensurability effects as well; however, it may also involve a competition between surface-induced microphase separation and bulk microphase separation. Simply stated, the wall will have less influence over the central region for larger systems than for smaller systems.

One could imagine that controlled χN annealing from below $(\chi N)_{MST}$ and $(\chi N)_S$ to a final value above $(\chi N)_{MST}$ and $(\chi N)_S$ could "magnify" the effects of the hexagonal well on microdomain ordering by allowing composition oscillations to slowly set in and eventually form a well-defined, partially microphase-separated surface layer, as referenced above. As $(\chi N)_{MST}$ is crossed, the surface layer will encourage further ordering, and then once $(\chi N)_S$ is crossed, bulk microphase separation will occur throughout the inside of the hexagon. We study such an annealing situation below.

3.2. AB Annealed Simulations. As mentioned above, composition oscillations appear near the boundary for values of χN below $(\chi N)_{MST}$. In Figure 5, we present representative *equilibrium* density composition profiles for A-attractive ($\chi_w N = 17$) and B-attractive ($\chi_w N = -17$) walls at $\chi N = 12$ and $\chi N = 14$. Recall that $(\chi N)_{MST} \approx 14.75$ for our system with $f = 0.7$,

so these values of χN correspond to the homogeneous (disordered) phase. With the exception of χN, we used the exact same system and simulation parameters discussed above. Each of these simulations were run at fixed χN for $n_t = 20\,000$ field iterations. At $\chi N = 12$, we observe composition oscillations near the wall, even though the system has not undergone a bulk microphase separation, and at $\chi N = 14$, we identify well-defined microphase separation and ordering near the wall, again, even though the system has not undergone a bulk microphase separation. It is our hope to take advantage of surface-induced composition oscillations, microphase separation, and ordering by slowing annealing from below $(\chi N)_{MST}$.

In order to further examine surface-induced microphase separation and ordering effects, we developed a (relatively) slow χN annealing scheme. Specifically, we annealed χN from $\chi N = 12 < (\chi N)_{MST}$, through $(\chi N)_{MST}$ and $(\chi N)_S$, to the final value of $\chi N = 17$. We incremented χN by 0.25 every 500 SCFT time steps, beginning at $t = 500\Delta t$ and ending at $10\,000\Delta t$. This annealing rate and step size allowed the system to fully relax between steps in χN; accordingly, on the time scale of the χN increments, the system can be assumed to have reached a local equilibrium. After the χN annealing, we then further relaxed the system using the standard SCFT saddle point search at fixed $\chi N = 17$ until $n_t = 20\,000$. Well-defined surface-induced microphase separation was observed during the anneal [much like the example presented in Figure 5b and Figure 5d], and this ordered layer facilitated formation of a hexagonal lattice once $(\chi N)_S$ was crossed and bulk microphase separation occurred.

The result of the annealing runs for an A-attractive wall ($\chi_w N = 17$), a neutral wall ($\chi_w N = 0$), and a B-attractive wall ($\chi_w N = -17$) are presented in Figure 6. We note that in all three cases the χN annealing increased the width of the commensurability window compared to those presented in section 3.1. For the A-attractive wall, the commensurability window is given by $\Lambda_{61}(17) = [15.75, 17.75]$. For the neutral wall, the commensurability window is given by $\Lambda_{61}(0) = [17.25, 19.75]$. And finally, for the B-attractive wall, the commensurability window is given by $\Lambda_{61}(-17) = [17.75, 19.75]$. The χN annealing has effectively equalized the ordering effects of the A-attractive, neutral, and B-attractive walls.

For the annealed systems presented here, defects likely form as the result of direct incommensurability conditions. That is, for small or large systems, the elastic strain energy is too great to maintain a perfect lattice for the specific hexagon side length, and as a result microdomain defects form. If one were able to minimize the energy of distortion associated with a highly incommensurate confining hexagon, perhaps the width of the commensurability window could be increased further. In the next section, we examine the possibility of relieving chain stretching in the majority block coronas with a majority-block homopolymer additive, and thus potentially increase the width of the commensurability window.

3.3. AB + A Annealed Simulations. In this section, we examine the effects of adding an majority-block homopolymer (i.e., A homopolymer) to the AB + wall system studied above. The fraction of A homopolymer is fixed at $\varphi_h = 0.20$ so that 20% of the melt is A homopolymer, and the A homopolymer length is selected to be $\alpha = 0.35$. Given the obvious advantages of χN annealing, all simulations presented in this section were run using the χN annealing scheme outlined in section 3.2.

In Figure 7, we plot $\langle\sigma\rangle$ vs L for the AB + A blend with a A-attractive wall ($\chi_w N = 17$), a neutral wall ($\chi_w N = 0$), and an B-attractive wall ($\chi_w N = -17$). Qualitatively these results are

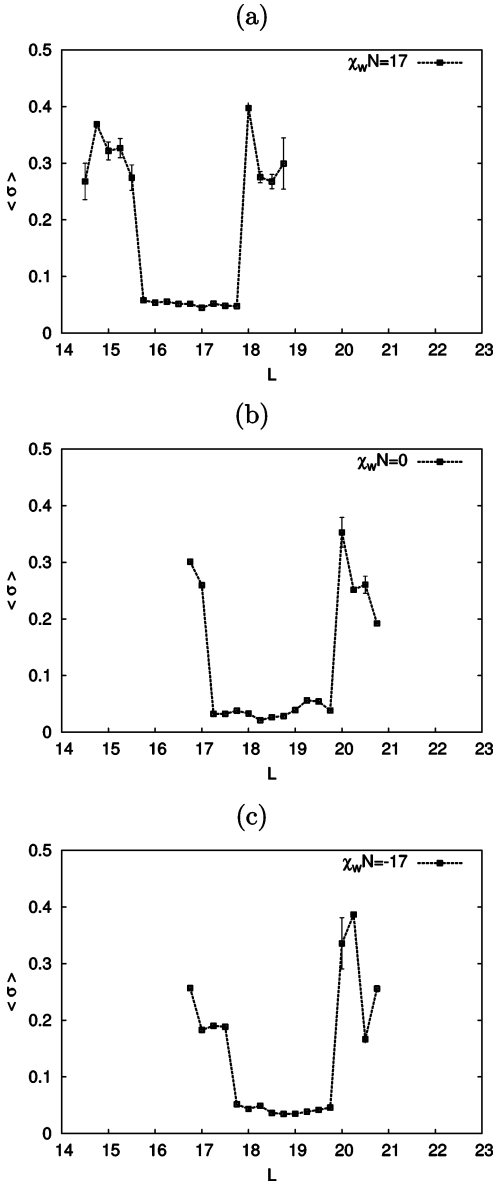

Figure 6. Graphs of $\langle\sigma\rangle$ vs L for an AB melt after a χN anneal from from random initial conditions at $\chi N = 12$ to $\chi N = 17$ for (a) an A-attractive wall ($\chi_w N = 17$), (b) a neutral wall ($\chi_w N = 0$), and (c) an B-attractive wall ($\chi_w N = -17$). Again, for each case, there is a commensurability window in L inside which there is a perfect array of 61 hexagonally ordered microdomains.

very similar to the those presented in Figure 6 for the AB melt; however, there are a few important differences. First of all, each of the commensurability windows in Figure 7 are shifted to larger values of hexagon side length L. This is because the matrix in the AB + A blend is swollen (as a result of the presence of the A homopolymer), resulting in a larger average NN distance for the ordered microphase. Specifically, with the addition of 20% A-homopolymer, the NN separations increased by approximately 6% for the A-attractive wall, 10% for the neutral wall, and 8% for the B-attractive wall. In addition, the commensurability window for the majority-block-attractive wall ($\chi N = 17$), illustrated in Figure 7a, is considerably smaller than for the annealed AB melt, illustrated in Figure 6a. This is because the A homopolymer tends to aggregate along the wall, producing an A-homopolymer surface layer. This layer is clearly visible in Figure 8a. The A homopolymer aggregation along the wall hinders the effectiveness of the A homopolymer at reducing chain stretching in the microphase matrix. In fact, the

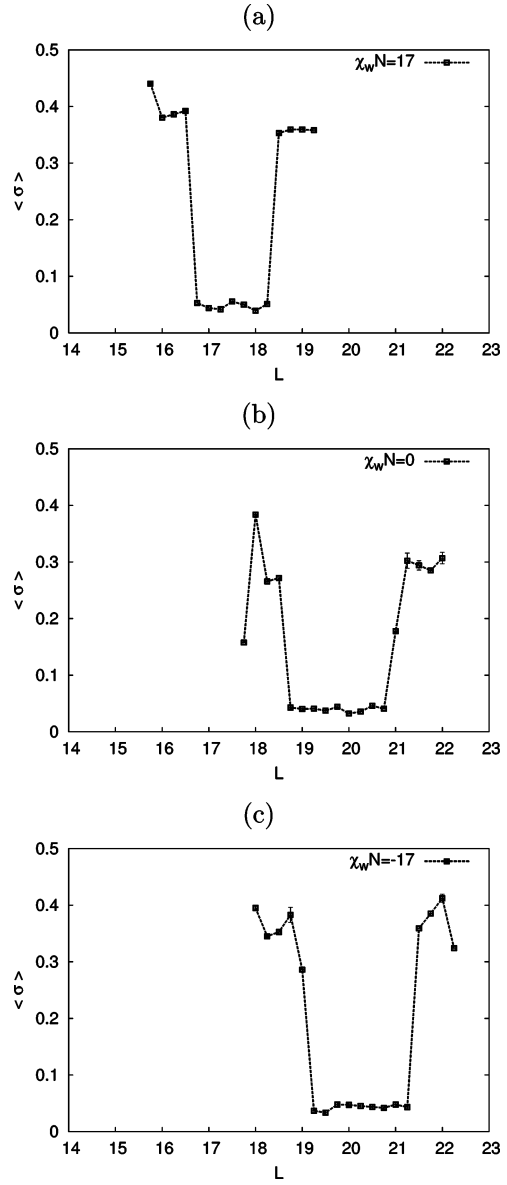

Figure 7. Graphs of $\langle\sigma\rangle$ vs L for an AB + A blend after a χN anneal from random initial conditions at $\chi N = 12$ to $\chi N = 17$ for (a) an A-attractive wall ($\chi_w N = 17$), (b) a neutral wall ($\chi_w N = 0$), and (c) an B-attractive wall ($\chi_w N = -17$). Again, for each case, there is a commensurability window in L inside which there is a perfect array of 61 hexagonally ordered microdomains.

aggregation appears to actually reduce the width of the commensurability window. On the other hand, from Figure 7, parts b and c, we can see that the commensurability windows for the neutral and minority-block-attractive walls appear to be about the same size as reported in section 3.2, albeit shifted to larger values of L. Furthermore, the homopolymer appears to be evenly distributed inside the hexagon for the neutral and B-attractive walls, as illustrated in Figure 8, parts b and c.

The slight shift in L for the commensurability windows may offer enough of a technological advantage to warrant incorporation of majority-block homopolymer in real-world studies of small-scale, lateral confinement of block copolymer systems—it allows one to achieve a high level of ordering (as measured with $\langle\sigma\rangle$) with larger confining hexagons. We suspect that a further shift and perhaps widening of the commensurability windows can be achieved by some subtle tuning of the hompolymer length α and segment fraction φ_h.

3.4. "Control" Case: 37 Enclosed Microdomains. In an attempt to test the validity of our observations and conclusions for other small-scale confinement sizes, we ran a parallel set of simulations, using exactly the same system parameters, except with a smaller hexagon size. The hexagon size was selected in order to yield seven rows of microdomains across the hexagon, or equivalently four microdomains along an edge. There are exactly 37 microdomains contained in such a confining hexagon. In order to conserve computer time, the simulations were carried out in a slightly smaller simulation space with $L_x = L_y = 36$ and $n_x = n_y = 144$. Otherwise, *all* system and simulation parameters were exactly the same as given above.

In qualitative terms, our observations appear to carry over to the case of 37 enclosed microdomains. We can see from Figure 9 that the relative positions and sizes of the commensurability windows, and the relative change in positions and sizes for the smaller confining hexagons agrees well with the observations reported in sections 3.1, 3.2, and 3.3.

For this smaller system, we also ran a series of 100 quenched simulations (using 100 different random initial conditions) for an A-attractive wall and a confining hexagon with $L = 13.00$ in the center of the commensurability window. Again, all other system and simulation parameters were the same as outlined above. The observed values of the standard deviation of nearest neighbor separations σ for the 100 different initial conditions were identical, and perfect ordering was achieved in each realization. This gives strong evidence that the observed order inside of the confining hexagon is highly reproducible.

3.5. Fluctuations. In this study, we used the mean-field, SCFT approximation to simplify our model. However, this approximation ignores (composition) field fluctuations that are otherwise present in the theory and are observable experimentally, e.g., near the order−disorder transition. It is quite possible

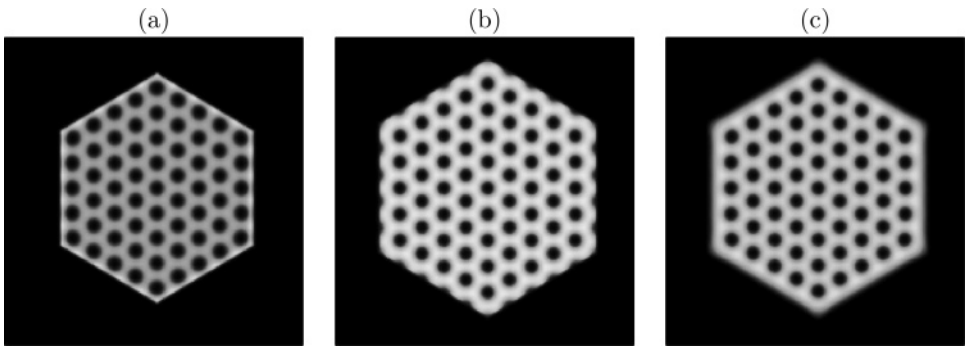

Figure 8. Representative composition profiles for an AB + A + wall system (lighter shades correspond to larger values of ϕ_{Ah}—the A homopolymer fraction) with (a) an A-attractive wall with $L = 17.50$, (b) a neutral wall with $L = 19.75$, and (c) a B-attractive wall with $L = 20.25$. The absolute shading is not important here, just the relative shading in each frame. In frame a, the area with the highest concentration of light shading is along the hexagon wall. This indicates that the A homopolymer is aggregating along the A attractive wall. For frames b and c, the A homopolymer concentration distribution appears to be much more uniform throughout the microphase matrix.

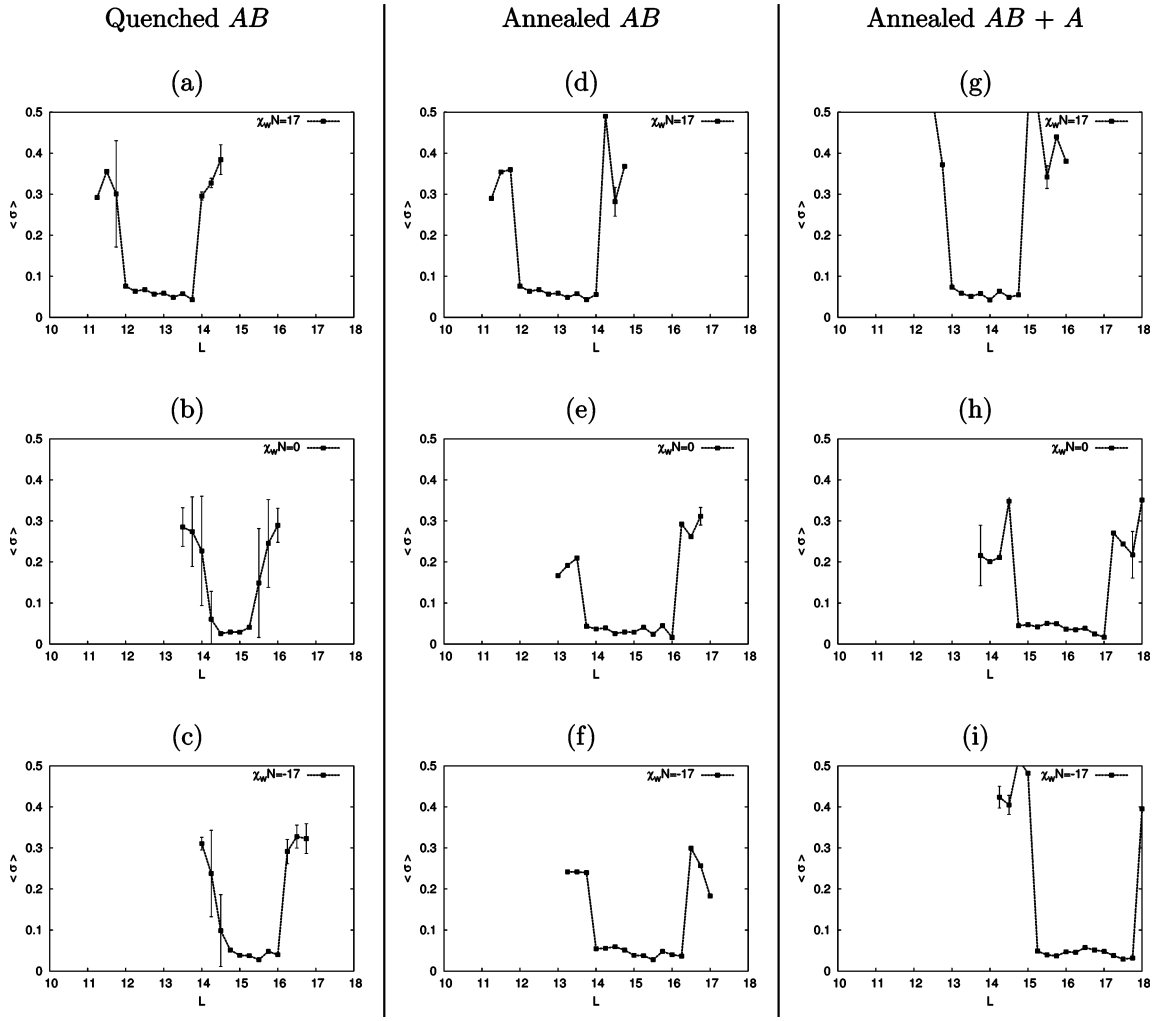

Figure 9. Graphs of $\langle\sigma\rangle$ vs L for various AB and AB + A systems with 37 enclosed microdomains (instead of the 61 enclosed microdomains reported in sections 3.1, 3.2, and 3.3). The first column (a−c) corresponds to the case presented in section 3.1 and Figure 1 for an AB melt quenched to $\chi N = 17$ with (a) an A-attractive wall, (b) a neutral wall, and (c) a B-attractive wall. The second column (d−f) corresponds to the case presented in section 3.2 and Figure 6 for an AB melt annealed from $\chi N = 12$ to $\chi N = 17$ with (d) an A-attractive wall, (e) a neutral wall, and (f) a B-attractive wall. The third column (g−i) corresponds to the case presented in section 3.3 and Figure 7 for an AB + A blend annealed from $\chi N = 12$ to $\chi N = 17$ with (g) an A-attractive wall, (h) a neutral wall, and (i) a B-attractive wall.

that composition fluctuations could affect the commensurability windows identified in this paper. For example, field fluctuations can serve to populate, as well as provide a path for escape from, low-energy defect structures. This competition could have an influence on the widths of the commensurability windows. In any event, the importance of fluctuations can be systematically controlled by varying the C parameter of section 2.1 (which varies with molecular weight as $C \sim N^{1/2}$) and eliminated in the $C \rightarrow \infty$ limit where the saddle point approximation becomes exact. For cases of finite C, fluctuation effects could be incorporated by implementing Monte Carlo or complex Langevin field-theoretic polymer simulation techniques.[20] Such simulation techniques, however, require considerably more computational resources than the SCFT methods utilized here.

4. Conclusion

We have examined the effects of small-scale, hexagonal, lateral confinement on ordering and defect formation in SCFT simulations of cylinder-forming block copolymer thin films. The confining well was modeled as a fixed density field that interacted with the segments via the melt incompressibility constraint and a Flory-type interaction term.

For a quench to $\chi N = 17$, a majority-block-attractive wall (in our case the A-attractive) had a larger effect on the ordering of the resulting microdomains than a neutral or minority-block-attractive wall. Specifically, for an A-attractive wall, the width of the commensurability window was 2.5 times larger than for the B-attractive wall and five times larger than for the neutral wall. This difference can be explained by examining the effects of surface-induced microphase separation phenomena near the MST and the spinodal.

Controlled temperature annealing from below $(\chi N)_{MST}$ to a final value of $\chi N = 17$ appears to equalize the effects of A-attractive, neutral, and B-attractive walls on ordering. This can be explained by observing the effects of significant composition oscillations that form below $(\chi N)_{MST}$ and, in turn, encourage improved ordering of the microphase once the bulk MST is crossed.

An A homopolymer (majority block) additive was examined as a means to increase the width of the commensurability windows. While no appreciable change in commensurability window width was observed for the 20% A homopolymer employed in our study, the added A homopolymer shifted the commensurability windows to larger values of L.

We have demonstrated that for hexagonal, laterally confined block copolymer thin films the preferential segment−wall interactions, hexagon side length, χN annealing rate, and polymer architecture and formulation *all* have an appreciable effect on the order of the enclosed microdomains. Moreover, we have shown that SCFT simulations can be fruitfully used to elucidate the role of each of these factors on the achievement of defect-free microdomain arrays.

The findings presented here could have technological relevance. In order to avoid the inherent difficulties of realizing large "single-crystal" arrays of BCP microdomains, one could instead pattern a surface with a grid of small hexagonal wells by using conventional top-down lithography. By filling the wells with block copolymer, and relying on bottom-up self-assembly, it should be possible to achieve a high degree of registry and uniformity of microdomains over macroscopically large areas. Inside of each hexagonal well would be a small-scale, well-ordered, uniform microdomain array such as the arrays presented in this paper.

Acknowledgment. The authors would like to thank Gila E. Stein, Edward J. Kramer, and Kirill Katsov for insightful discussions. The authors derived partial support from NSF grant DMR-0603710 and the MARCO Center on Functional Engineered Nano Architectonics (FENA). A.W.B. received additional support from The Frank H. and Eva B. Buck Foundation and the NRC/NIST Postdoctoral Research Associateship Program. The work of CJGC was funded in part by NSF Grant DMS-0505738. This work made use of MRL Central Facilities supported by the MRSEC Program of the National Science Foundation under Award No. DMR05-20415. In addition, we acknowledge use of the Hewlett-Packard cluster in the CNSI Computer Facilities.

References and Notes

(1) Park, C.; Yoon, J.; Thomas, E. L. *Polymer* **2003**, *44*, 6725.
(2) Segalman, R. A. *Mater. Sci. Eng. R* **2005**, *48*, 191.
(3) Cheng, J. Y.; Ross, C. A.; Smith, H. I.; Thomas, E. L. *Adv. Mater.* **2006**, *18*, 2505.
(4) Segalman, R. A.; Hexemer, A.; Hayward, R. C.; Kramer, E. J. *Macromolecules* **2003**, *36*, 3272.
(5) Segalman, R. A.; Hexemer, A.; Kramer, E. J. *Phys. Rev. Lett.* **2003**, *91*, 196101.
(6) Segalman, R. A.; Hexemer, A.; Kramer, E. J. *Macromolecules* **2003**, *36*, 6831.
(7) Angelescu, D. E.; Harrison, C. K.; Trawick, M. L.; Register, R. A.; Chaikin, P. M. *Phys. Rev. Lett.* **2005**, *95*, 025702.
(8) Kramer, E. J. *Nature (London)* **2005**, *437*, 824.
(9) Naito, K.; Hieda, H.; Sakurai, M.; Kamata, Y.; Asakawa, K. *IEEE Trans. Magn.* **2002**, *38*, 1949.
(10) Guarini, K. W.; Black, C. T.; Zhang, Y.; Kim, H.; Sikorski, E. M.; Babich, I. V. *J. Vac. Sci. Technol. B* **2002**, *20*, 2788.
(11) Black, C. T.; Guarini, K. W.; Zhang, Y.; Kim, H.; Benedict, J.; Sikorski, E.; Babich, I. V.; Milkove, K. R. *IEEE Electron Device Lett.* **2004**, *25*, 622.
(12) Cheng, J. Y.; Mayes, A. M.; Ross, C. A. *Nat. Mater.* **2004**, *3*, 823.
(13) Cheng, J. Y.; Zhang, F.; Smith, H. I.; Vancso, G. J.; Ross, C. A. *Adv. Mater.* **2006**, *18*, 597.
(14) Cheng, J. Y.; Zhang, F.; Chuang, V. P.; Mayes, A. M.; Ross, C. A. *Nano Lett.* **2006**, *6*, 2099.
(15) Hexemer, A.; Stein, G.; Kramer, E.; Magonov, S. *Macromolecules* **2005**, *38*, 7083.
(16) Stein, G.; Kramer, E.; Li, X.; Wang, J. *Phys. Rev. Lett.* **2007**, *98*, 086101.
(17) Stein, G.; Lee, W.; Fredrickson, G.; Kramer, E.; Li, X.; Wang, J. *Macromolecules* **2007**, *40*, 5791.
(18) Roerdink, M.; Hempenius, M.; Gunst, U.; Arlinghaus, H.; Vancso, G. *Small* **2007**, *3*, 1415.
(19) Stein, G. E.; Onikoyi, A.; Kramer, E. J. Private communication, 2006.
(20) Fredrickson, G. H. *The Equilibrium Theory of Inhomogenous Polymers;* Clarendon Press: Oxford, U.K., 2006.
(21) Matsen, M. W. *J. Chem. Phys.* **1997**, *106*, 7781.
(22) Fredrickson, G. H.; Ganesan, V.; Drolet, F. *Macromolecules* **2002**, *35*, 16.
(23) Fredrickson, G. H. *J. Chem. Phys.* **2002**, *117*, 6810.
(24) Maurits, N.; Fraaije, J. *J. Chem. Phys.* **1997**, *107*, 5879.
(25) Tzeremes, G.; Rasmussen, K. O.; Lookman, T.; Saxena, A. *Phys. Rev. E* **2002**, *65*, 041806.
(26) Rasmussen, K. O.; Kalosakas, G. *J. Polym. Sci., Part B: Polym. Phys.* **2002**, *40*, 1777.
(27) Sakurai, J. J. *Modern Quantum Mechanics*, *Revised Edition*; Addison Wesley: Reading, MA, 1994.
(28) Ceniceros, H. D.; Fredrickson, G. H. *Multiscale Modeling Simul.* **2004**, *2*, 452.
(29) Drolet, F.; Fredrickson, G. H. *Phys. Rev. Lett.* **1999**, *83*, 4317.
(30) Leibler, L. *Macromolecules* **1980**, *13*, 1602.
(31) Fredrickson, G. H.; Binder, K. *J. Chem. Phys.* **1989**, *91*, 7265.
(32) Hohenberg, P. C.; Swift, J. B. *Phys. Rev. E* **1995**, *52*, 1828.
(33) Fredrickson, G. H. *Macromolecules* **1987**, *20*, 2535.
(34) Tang, H.; Freed, K. F. *J. Chem. Phys.* **1992**, *97*, 4496.
(35) Turner, M. S.; Rubinstein, M.; Marques, C. M. *Macromolecules* **1994**, *27*, 4986.
(36) Brown, G.; Chakrabarti, A. *J. Chem. Phys.* **1994**, *101*, 3310.
(37) Binder, K. *Acta Polym.* **1995**, *46*, 204.
(38) Binder, K.; Frisch, H. L.; Stepanow, S. *J. Phys. II* **1997**, *7*, 1353.
(39) Throughout this paper we will often use the terms "A block" and "majority block" interchangeably. Clearly, the identification of the majority block depends on the specification of f; however, in this study the value of f is fixed at $f = 0.7$ and thus we identify the A block as the majority block.
(40) This total run time estimate does *not* include the test/control runs with 37 enclosed microdomains presented in section 3.4. The results presented in section 3.4 required 855 additional simulations, each requiring approximately 4 h of runtime on a dedicated compute node. This amounts to an additional 3420 compute-hours for a total of 9965 total compute-hours (equal to approximately 415 compute-days).

MA071866T